An IDDES study of the near-wake flow topology of a simplified heavy vehicle

Citation for the original published paper (version of record):
Zhang, J., Guo, Z., Han, S. et al (2022). An IDDES study of the near-wake flow topology of a simplified heavy vehicle. Transportation Safety and Environment, 4(2).
http://dx.doi.org/10.1093/tse/tdac015

(article starts on next page)

Transportation Safety and Environment, 2022, **4**: tdac015

DOI: 10.1093/tse/tdac015

Research Article

An IDDES study of the near-wake flow topology of a simplified heavy vehicle

Jie Zhang[1,2,3], Zhanhao Guo[1,2,3], Shuai Han[1,2,3], Siniša Krajnović[4], John Sheridan[5] and Guangjun Gao[1,2,3,*]

[1]Key Laboratory of Traffic Safety on Track of Ministry of Education, School of Traffic & Transportation Engineering, Central South University, Changsha 410075, China;

[2]Joint International Research Laboratory of Key Technology for Rail Traffic Safety, Central South University, Changsha 410075, China;

[3]National & Local Joint Engineering Research Center of Safety Technology for Rail Vehicle, Central South University, Changsha 410075, China;

[4]Department of Mechanics and Maritime Sciences, Chalmers University of Technology, Gothenburg 41296, Sweden;

[5]Department of Mechanical and Aerospace Engineering, Monash University, Clayton, Victoria 3800, Australia.

*Corresponding author. E-mail: gjgao@csu.edu.cn

Abstract

The complex wake flow of a GTS (ground transportation system) model contributes to large percentage of the aerodynamic drag force. Therefore, predicting accurate wake flow will help carry out the drag reduction strategies. In this paper, the near-wake flow topology of the GTS was studied at $Re = 2.7 \times 10^4$ to assess the capability of a hybrid RANS/LES (Reynolds-averaged Navier–Stokes/large eddy simulation) approach, known as IDDES (improved delayed detached eddy simulation). The current study also aims to understand the effects of different computational parameters, e.g. the spatial resolution, time step, residual level, discretization scheme and turbulence model, on this asymmetrical wake flow configuration. A comparison of IDDES with previous water channel tests, well-resolved LES, partially averaged Navier–Stokes and URANS (unsteady RANS) was included to better understand the benefits of this hybrid RANS/LES approach. The results show that on the medium and fine grids, the IDDES produces an asymmetrical flow topology (known as flow state I) in the near-wake of the vertical midplane, as reported in previous studies. The recommended parameters for the time step (1×10^{-4} s) and residual level (1×10^{-4}) provide sufficient accuracy of wake predictions to show good agreement with experiments. For the convective term of the momentum equation in IDDES, the bounded central difference discretization scheme is proposed to be adopted for discretization. Additionally, URANS cannot accurately capture this asymmetrical flow field. IDDES proves to be capable of predicting the wake flow field of this simplified heavy vehicle with high accuracy. All obtained conclusions can provide references for the aerodynamic drag reduction of the GTS.

Keywords: Heavy vehicle, Asymmetrical wakes, IDDES, Computational parameter

1. Introduction

Recently, a series of experimental and numerical investigations were performed on the ground transportation system (GTS), a model (originally designed by Sandia National Laboratories [1, 2]) was used to study the aerodynamics of heavy vehicles in the transportation industry. In the vertical midplane, different flow states were observed behind the GTS. McArthur et al. [3] experimentally observed a triangular-shaped vortex near the base, with an elliptical-shaped vortex above this but further away from the base (see Fig. 5(a) of Ref. [3]). However, the large eddy simulation (LES) results of Ref. [4] are antisymmetric to those of Ref. [3] in the wake of GTS (see Figs. 5(a)–(b) of Ref. [4]). In addition, Rao et al. [5] artificially realized the switching process from one flow state to another through numerical methods. Among these processes, an intermediate flow state of short duration (see Figs. 12 and 13 of Ref. [5]) can be observed, that is, a pair of symmetrical vortices. For convenience, the configuration observed in Ref. [3] is denoted as flow state I and its antisymmetry as flow state II.

For the GTS flow fields, the US Department of Energy studied the possibility of using computational fluid dynamics (CFD) to estimate the ability of turbulence models to predict the flow field around the GTS without yaw [6, 7]. Turbulence model tests included the Reynolds-averaged Navier–Stokes (RANS) Spalart-Allmaras (S-A), Wilcox k-ω and Menter k-ω models. They observed that the wake flow structures predicted by these models are significantly different from those seen in the experiments of Ref. [8]. At yaw angles, the simulations on the GTS flow fields using S-A RANS and detached eddy simulation (DES) turbulence models were carried out by Maddox et al. [9], which also shows a large discrepancy. All of this could be attributed to the limitations of the CFD technology at that time.

Since then, more studies on the wake flow structures of the GTS have been conducted. Ortega et al. [10] conducted LES on the GTS with only a rear portion, and the results again revealed differences in the structure of the wake region (similar to flow state II). They inferred this may be caused by truncating the model or neglecting the model supports. Following this, other DES and RANS simulations, e.g. unsteady RANS (URANS) renormalization group (RNG) k-ε model and DES by Unaune et al. [11], RANS Menter k-ω models by Roy et al. [12] (with Reynolds number different from that of Ref. [7]), RANS Realizable k-ε model by Ghias et al. [13] (comparing the body-fitted and immersed boundary method) and DES by Roy and Ghuge [14] (marching time is different from the studies of Refs. [9] and [11]), were compared with experiments, and still showed different flow topology (basically symmetrical in the wake). However, Gunes [15], using the URANS RNG k-ε model (the boundary layer mesh is used on the tunnel walls and cylinder supports, where more grids are concentrated), observed the

Received: November 29, 2021. **Revised:** February 7, 2022. **Accepted:** March 1, 2022

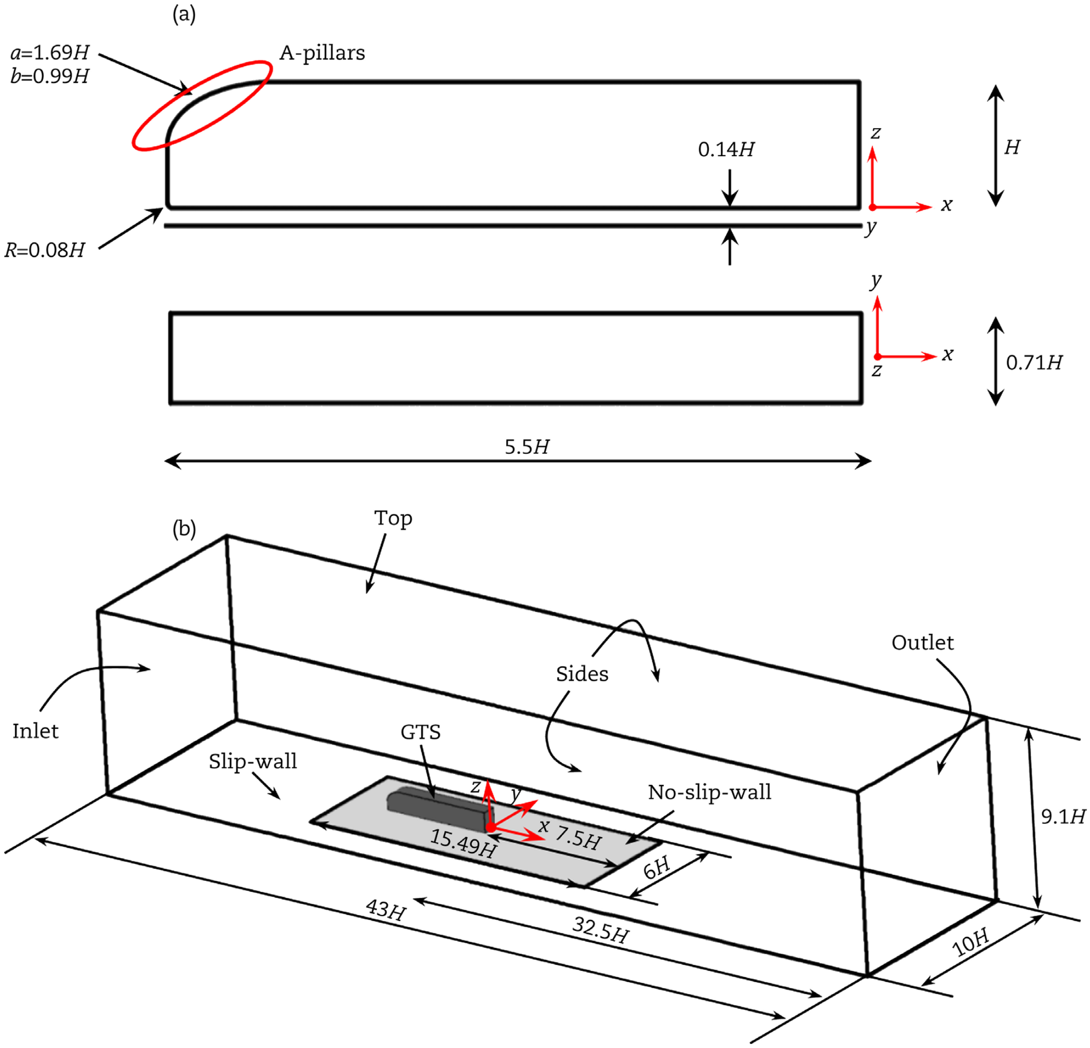

Fig. 1. Details of grids: (a) GTS model; (b) Computational domain.

asymmetry in the wake flow structures (similar to flow state I), and thought this is produced by the interaction between the Von Kármán vortices behind the cylinder supports and the wake of GTS. All these studies aim to accurately capture the flow structures observed in the experiments.

To obtain more details of this flow structure of GTS for future studies, an experiment was conducted by McArthur et al. [3]. Associating this flow topology with the previous research [16–23], Rao et al. [4] carried out LES simulations and inferred the existence of bi-stable states on the GTS model. The first observation of this bi-stable phenomenon can be tracked back to the experiment of Ref. [16].

The two flow states or the switching between them occur at random intervals [16, 24, 25], but only one of them can be observed in the numerical simulations because of the relatively short physical run-times compared with the experiments. For example, the flow topologies in Refs. [8], [15] and [3] are similar to flow state I; but those in Refs. [10] and [14] are antisymmetric (flow state II). As confirmed by Unaune et al. [11], Roy et al. [12] and Ghias et al. [13], some turbulence models cannot accurately predict this typical asymmetrical flow topology. PANS (partially averaged Navier–Stokes), a hybrid RANS/LES approach with different differencing schemes, was used to assess its application on this GTS flow [5], and achieved a successful flow prediction. Studying the effect of aspect ratio on this flow, a 9% maximum difference was found between the centre positions of the vortices of RANS $k-\omega$ model and the PANS at the original aspect ratio of 1.41 [26].

The improved delayed detached eddy simulation (IDDES) is an updated hybrid RANS/LES approach, designed to resolve the mismatch between the modelled log layer and the resolved log layer that are common in DES and delayed detached eddy simulation (DDES) [27–29]. The IDDES has been widely used in predicting the flow fields around streamlined bodies [30–34] and bluff bodies [35–37], with success in predicting the flow. However, from the results of Refs. [9], [14] and [11], the original DES model is not successful in predicting this flow topology of the GTS model. Therefore, it is necessary to verify the ability of IDDES to predict this flow topology, and to clarify how the chosen computational parameters influence the results. The aims of this study are to assess the capability of IDDES in predicting the near-wake flow topology of the GTS model, and to understand the effects of grid, time step, convergence criterion and differencing schemes on this flow configuration.

2. Methodology

2.1 Model description

The model, represented at a generic 1:40 scale Class-8 van-type tractor trailer geometry, was originally introduced in the previous water channel tests in Ref. [3], as shown in Fig. 1(a), with length

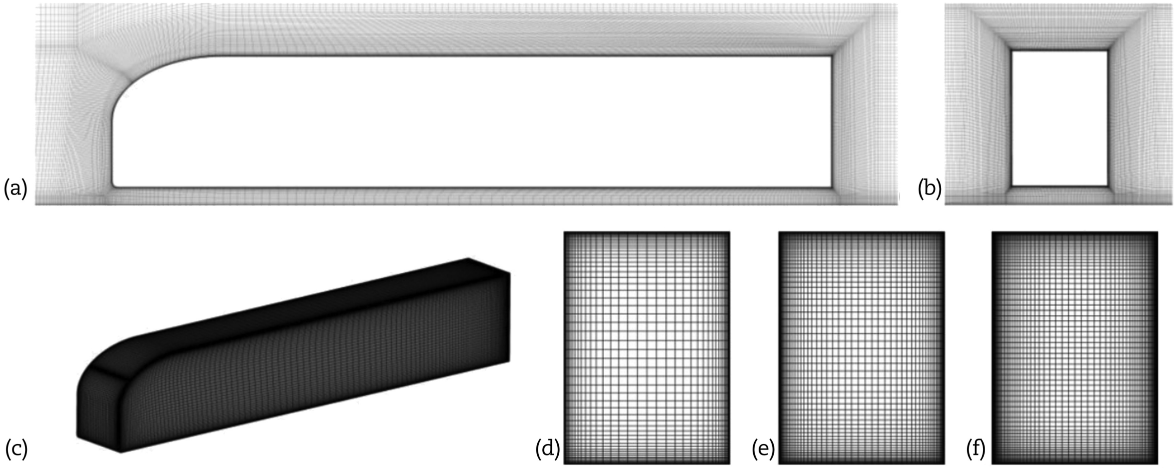

Fig. 2. Visualization of fine mesh distributions: spatial mesh around the GTS in the (a) vertical midplane; (b) YZ plane at $X/H = -1.95$; (c) GTS surface mesh distribution and different surface grid distributions on the base of the GTS: (d) coarse; (e) medium; (f) fine mesh.

$L = 0.495$ m, width $W = 0.064$ m and height $H = 0.090$ m. The front curved A-pillars of the model are replaced with a sharp-edged elliptical profile (long edge $a = 1.69H$, short edge $b = 0.99H$) to help the construction of the hexahedral mesh. In experiments, cylindrical or streamlined supports are usually used to fix the GTS model on ground, which will lead to the disturbance of the flow field under the GTS and make the wake flow field deviate to a certain flow state [16]. However, these were not used for the model considered here, to obtain an unperturbed underbody flow. The bi-stable phenomenon has been observed in the vertical midplane of parallelepiped bodies with an aspect ratio (height-to-width) of 1.34 and a ground clearance ratio (ground clearance-to-width) of 0.11, as reported by the experimental results in Ref. [16]. In the current case, although the front shape of the GTS is different from the model used by Grandemange et al. [16], the height-to-width ratio $H/W = 1.406$ gives a high chance to observe a similar bi-stable phenomenon in the vertical midplane (here, the ground clearance ratio is 0.2, which shows an ignoring influence when $C/W > 0.1$ in Ref. [16]). The computational domain and the location of the GTS model were designed to minimize the effects of the blockage ratio ($R \leq 1\%$) on the flow topology around the GTS, shown in Fig. 1(b). In the ground boundary condition, a slip wall enclosing a no-slip wall was used to reproduce the experimental set-up in Ref. [3]. The top and two sides were assigned as symmetry conditions. To obtain the same Reynolds number as the experiment ($Re = 2.7 \times 10^4$), the inflow velocity was set as $U_{\text{in}} = 6.16$ m/s at the inlet. To keep consistent with the water channel tests, the width (W) of the GTS is used as the reference length to calculate the Reynolds number; however, all other quantities are normalized by its height (H) if not stated otherwise. The outlet was treated as the pressure-outlet boundary condition.

2.2 Spatial resolution

In this study, three hexahedral meshes were constructed by commercial grid generator software Ansys ICEM CFD 19.2, i.e. coarse, medium and fine meshes, consisting of about 1.00, 5.10 and 8.45 million cells, respectively. On the fine mesh, the spatial grid distributions in the symmetry plane and YZ plane at $X/H = -1.95$ are shown in Figs. 2(a) and (b), respectively, while the surface grid distribution of the GTS is shown in Fig. 2(c). Figs. 2(d)–(f) show the surface grid distributions on the base of the GTS in the different meshes, respectively.

Table 1. Details of computational grids.

Parameter	Coarse	Medium	Fine
n^+_{mean}	<1	<1	<1
Δs^+_{max}	<290	<150	<100
Δl^+_{max}	<140	<50	<35
Number of cells (million)	1	5.1	8.45

Table 1 lists the details of the three grids. Here, n^+ is the dimensionless wall distance defined as $n^+ = nu_\tau/\nu$, where n is the normal distance from the GTS surface to the first node and u_τ is termed the friction velocity. Similarly, for the streamwise and spanwise directions the dimensionless lengths are calculated by $s^+ = \Delta s u_\tau/\nu$ and $l^+ = \Delta l u_\tau/\nu$, respectively. Here, Δs and Δl are the surface grid spacing in the streamwise and spanwise directions, respectively.

2.3 Computational parameters

The commercial CFD solver ANSYS Fluent 19.2 with an IDDES approach based on the SST (shear stress transport) k-ω turbulence model is used. The velocity and pressure corrections are achieved by SIMPLEC (semi-implicit method for pressure-linked equations consistent). The discretization scheme for the convective terms of the turbulence transport equations is the second-order upwind scheme. However, the convective terms of the momentum equations are discretized by the bounded central differencing scheme (recommended by solver). Besides, in subsection 3.4, to check the effect of discretization schemes, the second-order upwind scheme is tested and compared with the results of the bounded central differencing scheme. For transient simulations, the transient terms are approximated by the bounded second-order implicit scheme. A simulation is considered converged when the residual level in the domain falls below a desired tolerance. In addition, in subsection 3.3, the sensitivity of the residual level on the wake flow topology is investigated. In subsection 3.2, to assess the impact of CFL (Courant-Friedrichs-Lewy) on the wake flow topology, different time steps are used.

In all cases, a fully developed flow field can be of great benefit to IDDES unsteady simulation, so the steady simulation was first performed to fully develop the flow. After switching to IDDES, the instantaneous flow field is required to reach the statistically averageable state before gathering the unsteady statistics.

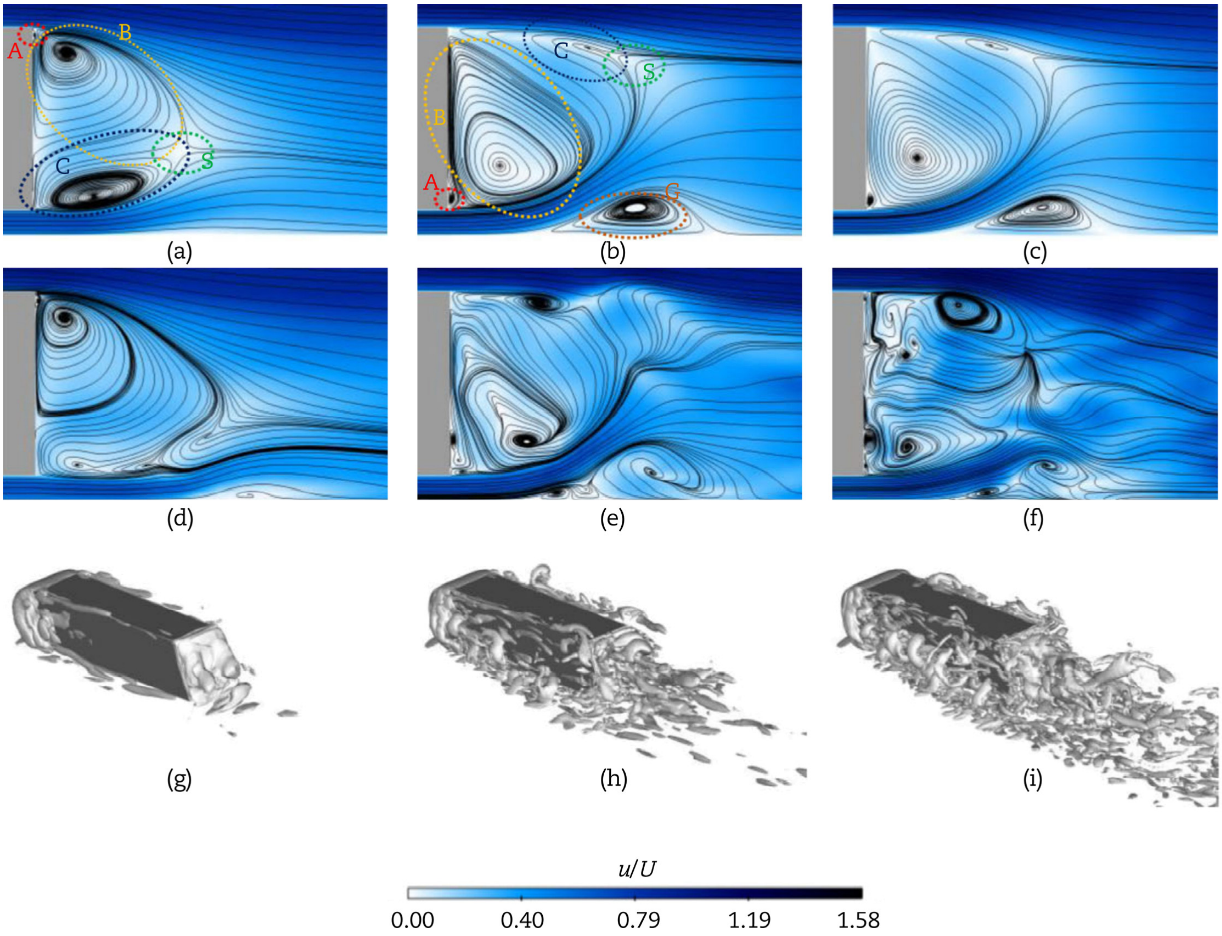

Fig. 3. The normalized time averaged velocity field for (a) coarse mesh, (b) medium mesh, (c) fine mesh; the normalized instantaneous velocity field for (d) coarse mesh, (e) medium mesh, (f) fine mesh; the iso-surface of Q-criterion ($Q = 1\text{x}10^4\ s^{-2}$) for (g) coarse mesh, (h) medium mesh, (i) fine mesh.

Therefore, the statistical sampling was started after three flow-through (from the inlet to the outlet) times. To ensure a sufficiently long sampling period, another three flow-through times were used for sampling.

The work in the current paper can be summarized as follows. Firstly, the numerical set-ups of the base case are fixed according to the long experience in performing time-dependent simulations of bluff body flows in our research group. After that, the effects of the grid resolution, time step, residual level and momentum discretization scheme are discussed in each subsection. Finally, the results of IDDES are used to compare with those of URANS to confirm that for this asymmetrical wake flow there are benefits in adopting an IDDES approach.

3. Results and discussion

The influences of the grid resolution, time step, residual level and momentum discretization scheme on the wake flow topology are discussed herein. The evaluation is based on the normalized time-averaged and instantaneous velocity field, iso-surfaces of Q-criterion, the pressure coefficient distribution on the base, the iso-surfaces of the pressure coefficient, the time-averaged vortex centres, the streamwise velocity and vertical velocity profiles, the distribution of Reynold stresses and the time-averaged force coefficients of the GTS model.

3.1 Influence of grid resolution

To study the effect of grid spatial resolution (see Table 1) on the flow structures around the GTS, the computational parameters for each case remain fixed with the time step $\Delta t = 1\times10^{-4}$ s, residual level of 1×10^{-4} and the same discretization schemes (unsteady terms: the bounded second-order implicit scheme; momentum equation: the bounded central differencing scheme; turbulence transport equations: the second-order upwind scheme). Figs. 3(a)–(c) show the time-averaged velocity field on the symmetric plane at $y = 0$. With the coarse grid, a slight asymmetric flow structure is observed, as shown in Fig. 3(a), with the saddle point S below the half height of the GTS; a larger triangular vortex B is located on the upper side, whereas the other narrow and stretched vortex C is on the lower side. This asymmetric flow topology shows a similarity, but with a light asymmetry, compared to Figs. 5(a)–(b) of Ref. [4]. On finer grids, as shown in Figs. 3(b)–(c), the wake flow structures, known as flow state I, are consistent with those of Ref. [3].

For the instantaneous flow shown in Figs. 3(d)–(f), all velocity field are visualized at the instant of $t = 2.0$ s (normalized time $T = \Delta t U_{\text{in}}/H = 274$, and all snapshots below are taken at this instant). The general observation is that the location of the main instantaneous vortices remains consistent with those in the mean flows. At the rear, with the coarse grid, the instantaneous flow structure is relatively regular, further indicating that the inadequate grid resolution leads IDDES to act as URANS. A series of vortices attached on the ground is also observed on the three grids, but

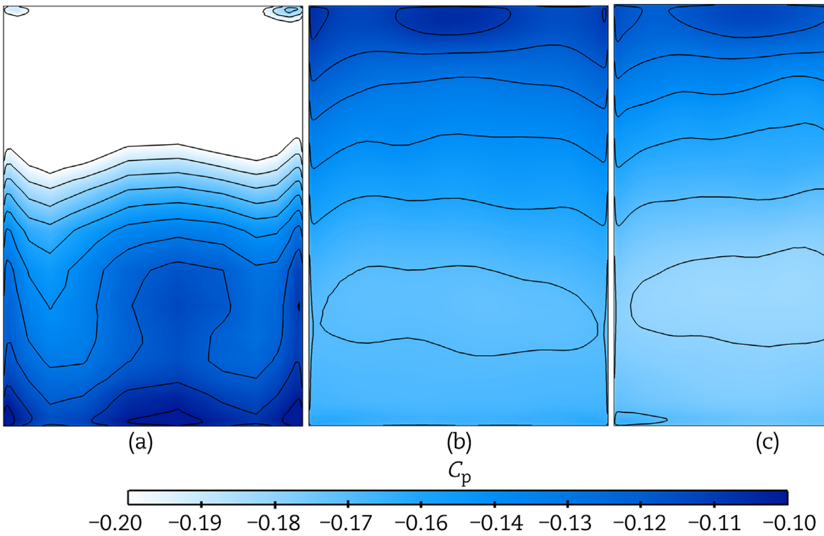

Fig. 4. Mean C_p distribution on the base for (a) coarse, (b) medium and (c) fine mesh.

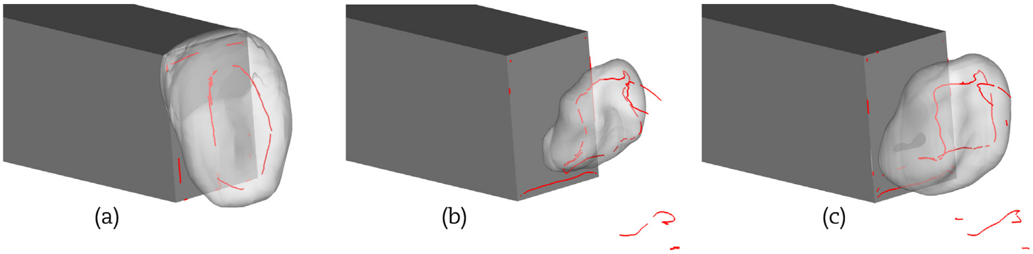

Fig. 5. Visualization of the iso-surfaces of pressure coefficient C_p for (a) coarse mesh; $C_p = -0.18$; (b) medium mesh, $C_p = -0.18$; (c) fine mesh, $C_p = -0.18$. (The red lines indicate the time-averaged vortex cores.)

there are not evidently shown at the time-averaged velocity field in the coarse grid. With a finer grid, there are more tiny vortices and the dominant ones are observed in the instantaneous snapshots. The iso-surfaces of the Q-criterion on three grids are shown in Figs. 3(g)–(i). The IDDES using a coarse grid only resolves the large-scale flow structures (see Fig. 3(c)). With grid refinement, more flow structures are resolved and captured, particularly in the separated flow regions besides the GTS and in the wake.

The contours of the pressure coefficient $C_p = p/(0.5\rho U_{in}^2)$ for different grids are shown in Fig. 4. Here, p is the mean local pressure relative to the atmosphere, and ρ is the air density (1.225 kg/m^3). As shown in Fig. 3(a), for the coarse grid, due to the close proximity between the triangular vortex and the upper base, there is a low-pressure region at the upper part and a higher-pressure region at the bottom. However, on the medium and fine grids, the high-pressure and low-pressure regions appear at the upper and bottom parts, respectively, and the corresponding pressures are slightly higher and lower than those on the coarse grid, resulting in the pressure distributions on the base being more even.

Fig. 5 shows the pressure coefficient C_p torus on different grids. Herein, the shape of the slanted torus further confirms that asymmetrical flow field behind the GTS and the pressure distribution on the base. For the medium and fine grid resolutions, the bottom of the C_p torus is closer to the base, while for the coarse one, the upper part of the C_p torus tilts towards the base.

Fig. 6 shows the location of the wake vortex cores. According to the above analysis on different grid resolutions, two flow topologies are observed, as shown in Figs. 3–5. Thus, to make a clear comparison, the vortex locations are classified and compared. Specifically, the vortex locations from LES of Ref. [4] and PANS of Ref. [5] are shown together with those from the coarse grid case in Fig. 6(a), while the experimental data of Ref. [3] are listed together with those from the medium and fine grid cases in Fig. 6(b). In these figures, the denotation of vortexes is the same as that in Fig. 3. Vortex B is the large triangle attached by the tiny vortex A, while vortex C represents the smaller elliptical vortex. In addition, the ground vortex is denoted by vortex D, and the saddle point is marked by S.

In Fig. 6(a), the vortex centres on the coarse mesh are more approximate to the base of the GTS, but with larger differences compared to the LES of Ref. [4] and PANS of Ref. [5], indicating that the flow field predicted by the coarse IDDES is very difficult to classify as the flow state II of a bi-flow state. This phenomenon can be ascribed to the insufficient spatial resolution. As shown in Fig. 6(b), the vortex centres of the fine mesh are closer to the experiments than those of the medium mesh, while the saddle point of the fine mesh is not as close to the experiments as the medium mesh. To conclude, the vortex centres and saddle point, predicted by the medium and fine IDDES, show good consistency with the experiments of Ref. [3]. Thus, to balance the computational resource and accuracy, the medium mesh is used for the further study.

Fig. 7 compares the streamwise and vertical velocity profiles of all three grids from the base to $X/H = 2$ with an interval of $0.25H$. In these figures, the X coordinate is calculated as follows: $X = x_o+((u/U_{in})-1)\times 0.01$. Here, x_o is the x coordinate. u can be

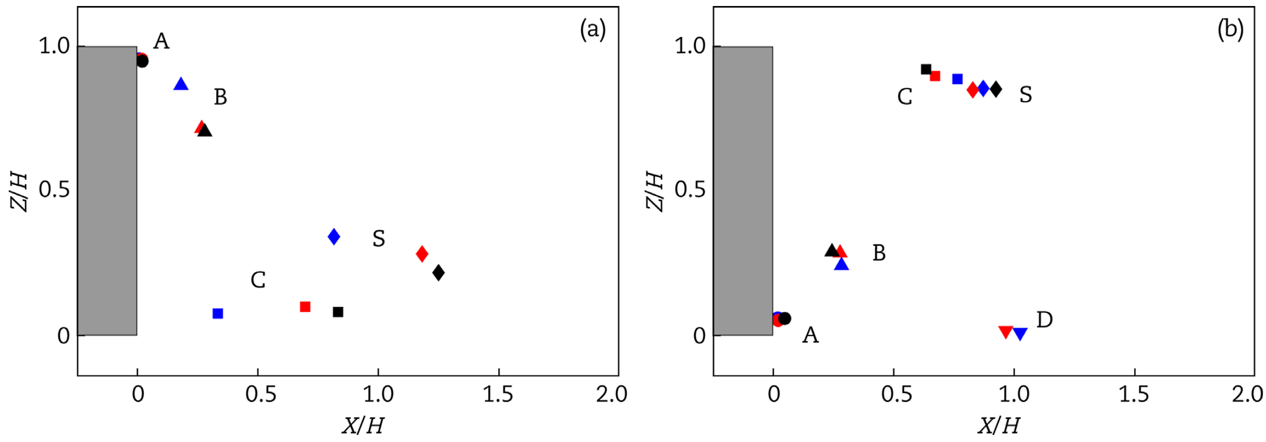

Fig. 6. Centre locations of the time-averaged vortices: (a) the coarse mesh (blue) is compared with the LES [4] (red) and the PANS [5] (black); (b) the medium mesh (blue) and the fine mesh (red) are compared with the experiments [3] (black). (The marker with the same shape represents the corresponding vortex or saddle point. The comparison cases are all carried out at the same Reynolds number.)

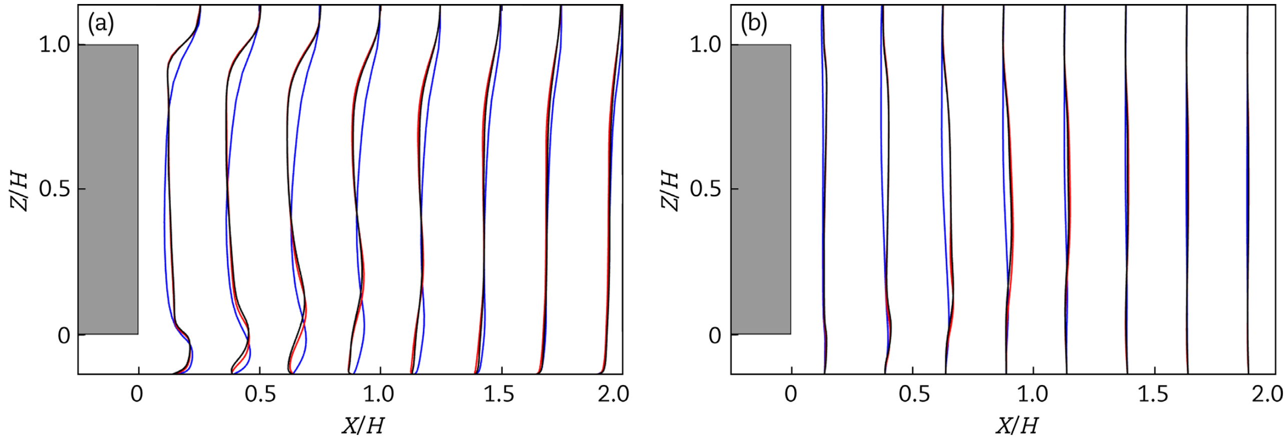

Fig. 7. Comparison of (a) streamwise velocity and (b) vertical velocity profiles. (The blue, red and black lines correspond to the coarse, medium and fine mesh, respectively.)

replaced by the mean streamwise u_x and vertical u_z velocities, respectively. From the above analysis, the flow topology of the coarse mesh is approximately antisymmetric to those of the medium and fine meshes. Therefore, there is a large discrepancy in velocity distribution between the coarse mesh and the medium/fine meshes, while good consistency of the results is observed between the medium and the fine meshes.

The normalized Reynolds normal stresses distributions are shown in Fig. 8 with the same colourmap as Fig. 9 of Ref. [3]. Here, u'_x and u'_z are the fluctuating velocity in the x and z directions, respectively. $\langle u'^2_{x,\,z}\rangle$ is the Reynolds stress and $\langle u'^{*2}_{x,\,z}\rangle$ is the Reynolds stress normalized by the inflow velocity. On a finer mesh, the distribution of the Reynolds stresses are similar to Fig. 9 of Ref. [3], except that the intensity of the Reynolds stress around the ground vortex is larger than that observed in the experiment. The distribution of $\langle u'^{*2}_x\rangle$ is mainly located along the upper and lower shear layers (Figs. 8(b) and (c)), and the peak of the vertical fluctuations $\langle u'^{*2}_z\rangle$ occurs around the saddle point, where the vorticity transported from the lower shear layers is interacting with that from the upper shear layers (Figs. 8(e) and (f)). The regions of high $\langle u'^*_x u'^*_z\rangle$ are similar to that of $\langle u'^{*2}_x\rangle$ (Figs. 8(h) and (i)), and the sign of $\langle u'^*_x u'^*_z\rangle$ just indicates that the main fluctuations are directed towards the saddle point at an inward angle. However, in the coarse mesh, both the Reynolds normal stresses and shear stresses occur along the lower shear layer and near the saddle point (Figs. 8(a), (d) and (g)).

Table 2 lists the time-averaged drag and lift coefficients experienced by the GTS on these three meshes, and compares them with those in LES [4] and PANS [5]. In this study, the mean force coefficients in the x and z directions are defined as $\langle C_x\rangle=\langle F_x\rangle\,/(0.5\rho U^2 S)$, $\langle C_z\rangle=\langle F_z\rangle\,/(0.5\rho U^2 S)$, where $\langle F_x\rangle$ and $\langle F_z\rangle$ are the sum of the mean viscous force and differential pressure force in the x and z directions, respectively, while S is the base area of the GTS (≅ 0.00576 m^2). The observation is that the forces predicted by IDDES are consistent with the data from LES, although the flow states are not the same. From the conclusion of Ref. [16], as the two states are almost symmetric, they are expected to present the similar drag. Therefore, compared with PANS, the IDDES for this GTS model shows higher accuracy of prediction at the same flow state I. Concerning the effect of grid resolution on the forces in IDDES: the $\langle C_x\rangle$ is around 0.56, while the $\langle C_z\rangle$ is -0.22. The coarse grid case has a lift force coefficient of -0.1657, which is significantly different when compared to the finer mesh. The difference of $\langle C_x\rangle$ and $\langle C_z\rangle$ between the medium mesh and fine mesh in IDDES is less than 3%, confirming that the medium mesh can be reliably used for the following study.

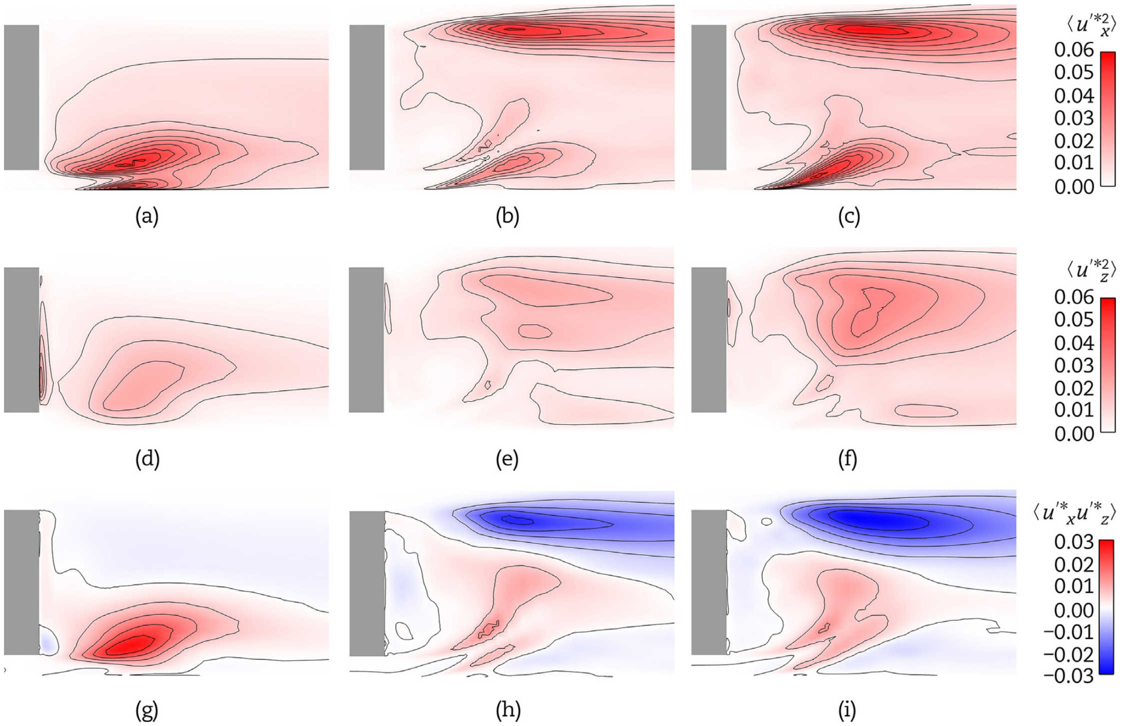

Fig. 8. The normalized Reynolds stresses distribution $\langle u'^{*2}_x \rangle$ for (a) coarse mesh, (b) medium mesh, (c) fine mesh; the normalized Reynolds stresses distribution $\langle u'^{*2}_z \rangle$ for (d) coarse mesh, (e) medium mesh, (f) fine mesh; the normalized Reynolds stresses distribution $\langle u'^{*}_x u'^{*}_z \rangle$ for (g) coarse mesh, (h) medium mesh, (i) fine mesh.

Table 2. Time-averaged force coefficients of the GTS model from current simulation, LES [4] and PANS [5]. In PANS, different differencing schemes are used: ASB (AVL Sharp and monotonic algorithm for realistic transport bounded scheme) and CDS (central differencing scheme).

Turbulence model	Number of cells (million)	$\langle C_x \rangle$	$\langle C_z \rangle$	Flow state
IDDES	1.00	0.5639	−0.1657	\
IDDES	5.10	0.5629	−0.2212	I
IDDES	8.45	0.5783	−0.2278	I
PANS-ASB	3.88	0.5091	−0.2120	I
PANS-ASB	8.35	0.5196	−0.2325	I
PANS-ASB	10.78	0.5294	−0.2319	I
PANS-CDS	3.88	0.4937	−0.1971	II
PANS-CDS	8.35	0.5076	−0.1920	II
PANS-CDS	10.78	0.5035	−0.1837	II
LES	3.88	0.5724	−0.1885	II
LES	8.35	0.5734	−0.2010	II
LES	10.78	0.5608	−0.1974	II

3.2 Influence of time step

To investigate the influence of time step on the flow topology around GTS, four simulations with different time steps were performed on the medium mesh: they are 5×10^{-5} s, 1×10^{-4} s, 2×10^{-4} s and 1×10^{-3} s. To ensure that the overall simulation time is consistent for different time steps, the corresponding numbers of time step have been adjusted.

In fact, the appropriate time step should be chosen to resolve important flow phenomena and retain the stability of the solution process. A related index is Courant number, which is equal to $U\Delta t/\Delta x$. Here, Δt is the time step and Δx is the reference cell length. A higher Courant number will lead to faster convergence, but the higher the value, the more unstable the solver process. For time-accurate simulations, the time step should maintain the Courant number at all cells below 1.0, i.e. fluid passing through no more than one cell length in one time step. Fig. 9 is the contours of Courant number at different time steps. At the time steps 1×10^{-4} s and 5×10^{-5} s, the high Courant number (>1.0) regions are mainly concentrated on the corner of the O-grid, where the time step cannot meet the requirement of the smaller cells. With increased time step, the regions of high Courant number increase. In particular, the regions of Courant number beyond 1.0 are almost distributed all around the GTS model at the time step of 1×10^{-3} s.

For the mean flow fields (as shown in Figs. 10(a), (d), (g) and (j)), the flow structures at different time steps are similar to the flow state I, and all structures are almost identical, except for the upper elliptical vortex core and saddle point at the time step of 1×10^{-3} s. The corresponding instantaneous flow fields, presented in Figs. 10(b), (e), (h) and (k), are basically consistent with the time-averaged ones. In addition, although a large time step (1×10^{-3} s) cannot capture the upper vortex in the time-averaged flow field, the relevant vortex can be observed in the instantaneous flow field. This is because the time step is so large that the fluid progresses so quickly in one time step that the time-filtered data results in the loss of some flow phenomena in the time-averaged flow field. This is further confirmed from the iso-surfaces of Q-criterion (as show in Figs. 10(c), (f), (i) and (l)). A smaller time step captures a wider range of the vortex structures, including important small-scale vortices.

Fig. 11 shows the mean C_p distribution at four time steps. Although sampling for a long time, as the time step reduces, the pressure on the base of the GTS does not show a regular distribution. For example, the base pressure distributions at time steps 1×10^{-3} s and 1×10^{-4} s are almost symmetric about the vertical symmetry plane, but at time steps 2×10^{-4} s and 5×10^{-5} s there is

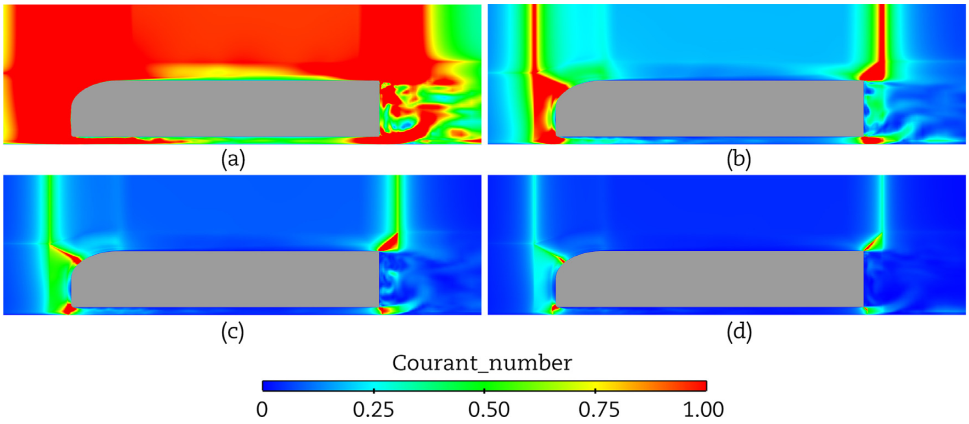

Fig. 9. Visualization of the contours of the Courant number for (a) time step of 1×10^{-3} s; (b) time step of 2×10^{-4}s; (c) time step of 1×10^{-4} s; (d) time step of 5×10^{-5} s.

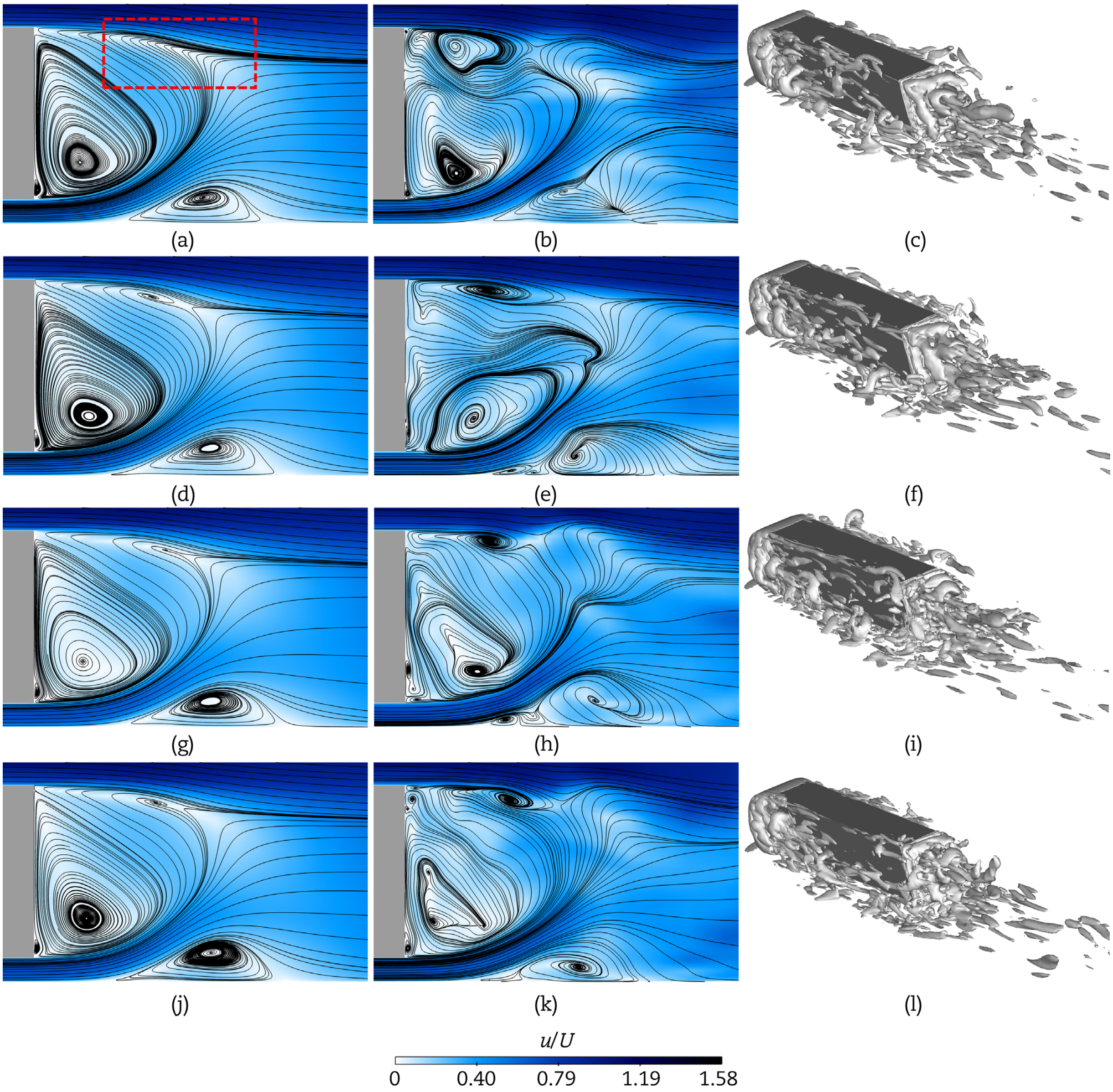

Fig. 10. The normalized time averaged velocity field for time step of (a) 1×10^{-3} s, (d) 2×10^{-4} s, (g) 1×10^{-4} s, (j) 5×10^{-5} s; the normalized instantaneous velocity field for time step of (b) 1×10^{-3} s, (e) 2×10^{-4} s, (h) 1×10^{-4} s, (k) 5×10^{-5} s; the iso-surface of Q-criterion ($Q = 1\times10^{4}$ s^{-2}) for time step of (c) 1×10^{-3} s, (f) 2×10^{-4} s, (i) 1×10^{-4} s, (l) 5×10^{-5} s.

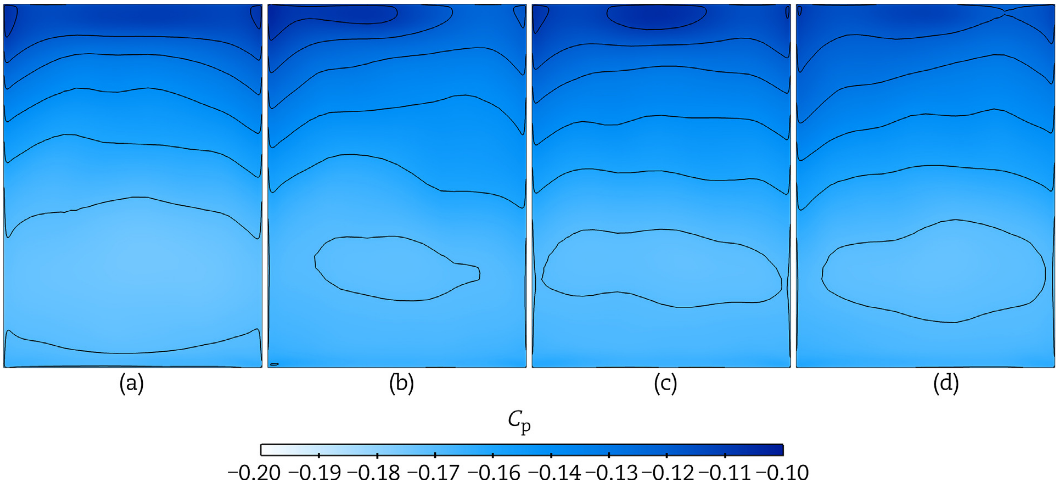

Fig. 11. Mean pressure coefficient C_p distribution on the base for (a) time step of 1×10^{-3} s; (b) time step of 2×10^{-4} s; (c) time step of 1×10^{-4} s; (d) time step of 5×10^{-5} s.

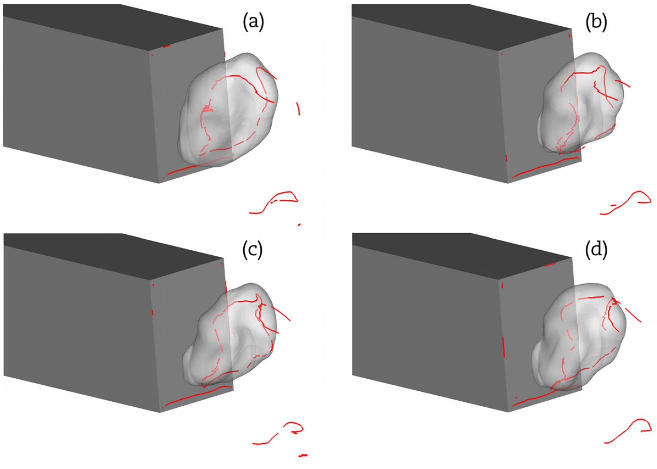

Fig. 12. Visualization of the iso-surfaces of the pressure coefficient C_p for (a) time step of 1×10^{-3} s; (b) time step of 2×10^{-4} s; (c) time step of 1×10^{-4} s; (d) time step of 5×10^{-5} s. ($C_p = -0.18$ in all these cases. The red lines indicate the time-averaged vortex cores.)

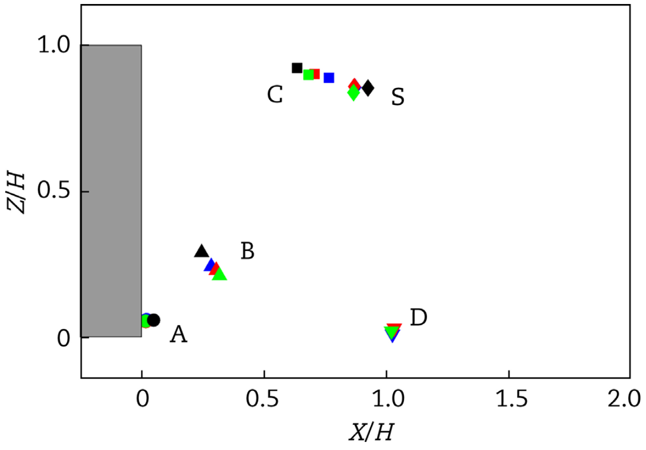

Fig. 13. Centre locations of the time-averaged vortices. The time step 5×10^{-5} s (red), the time step 1×10^{-4} s (blue), the time step 2×10^{-4} s (green), and the time step 1×10^{-3} s (pink) are compared with the experiments of Ref. [3] (black).

clear asymmetry, especially in the high-pressure region on the upper part. In addition, the low-pressure region on the base has large differences at different time steps. All these indicate the vortex behind the GTS might have strong transient characteristics, which also can be shown in the shape of corresponding C_p torus behind the GTS (see Fig. 12).

The vortex centres at different time steps in the vertical midplane are shown in Fig. 13. The upper elliptical vortex C and saddle point S cannot be predicted at the time step of 1×10^{-3} s and they are not shown in this figure. Except for the upper elliptical vortex C, the locations of the other vortex cores and saddle point at different time steps basically overlap, and the positions of vortex cores and saddle point captured by numerical simulations are all close to the experimental data in Ref. [3].

Fig. 14 compares the streamwise and vertical velocity distributions at four time steps. Also, the velocity profiles at different time steps are highly similar, except for the region around $Z/H = 0$, where the velocity gradient is relatively large, leading to different velocity variations captured by different time steps. Evidence of this is shown by comparing the results between the time step 1×10^{-3} s and the others.

Table 3 lists the mean drag and lift force coefficients at different time steps. The force coefficients found by the model for all time steps show good consistency with differences of only 2%. When the time step reduces to 2×10^{-4} s, the discrepancy is found to be less than 1% compared to the forces at the time step of 5×10^{-5} s. Thus, considering that the simulation using time step of 1×10^{-3} s results in the loss of partial flow topology and saving computational resources, the time step of 1×10^{-4} s was chosen for further analysis.

3.3 Influence of residual level

From conservation laws, the total flux of a general variable ϕ entering and exiting a given volume should be equal, but after discretization, there can be an imbalance. The total imbalance summed over all the computational cells P is referred as the 'unscaled' residuals. To judge convergence conveniently, ANSYS Fluent scales the residuals using scaling factors. The 'globally scaled' residual is defined as $R^{\phi} = \Big(\sum_{\text{cells P}} \big|\sum_{\text{nb}} a_{\text{nb}}\phi_{\text{nb}} + b - a_{\text{P}}\phi_{\text{P}}\big|\Big)/\Big(\sum_{\text{cells P}} |a_{\text{P}}\phi_{\text{P}}|\Big)$ [38]. Here, a_{P} is the

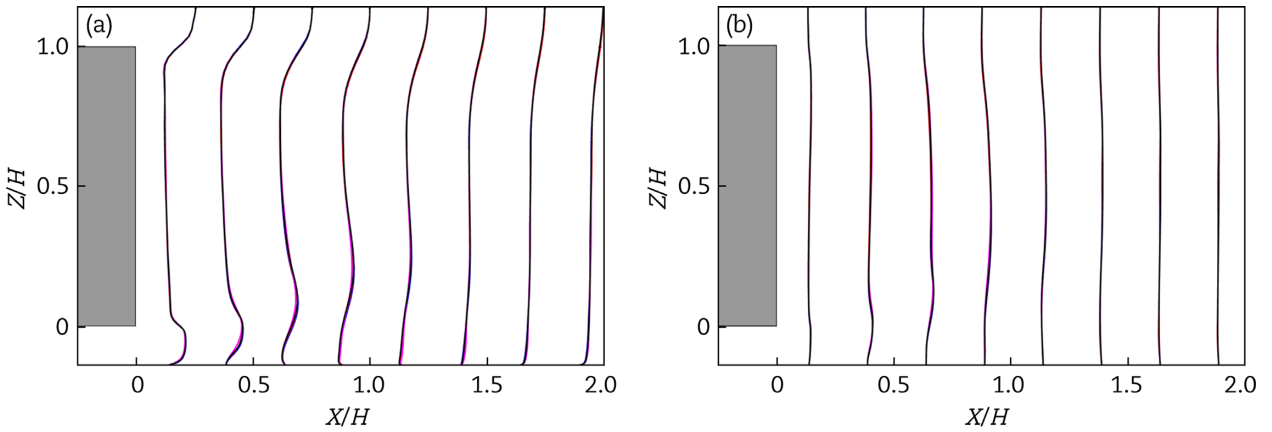

Fig. 14. Comparison of (a) streamwise velocity and (b) vertical velocity profiles. (The blue, red, black and pink lines correspond to the time steps of 5×10^{-5} s, 1×10^{-4} s, 2×10^{-4} s and 1×10^{-3} s, respectively.)

Table 3. Time-averaged force coefficients of the GTS model at different time steps.

Time step	$\langle C_x \rangle$	$\langle C_z \rangle$
1×10^{-3} s	0.5713	−0.2220
2×10^{-4} s	0.5674	−0.2210
1×10^{-4} s	0.5629	−0.2212
5×10^{-5} s	0.5631	−0.2209

centre coefficient, a_{nb} is the influence coefficients for the neighbouring cell and b is the contribution of the constant part of the source term and the boundary conditions [38]. For different solvers or transport equations, the formula has different forms, but the meaning is almost the same. The residuals indicate how well the discretized equation is satisfied. In this study, the 'globally scaled' residuals in Pressure-Based solver in ANSYS Fluent are used.

To study the satisfaction of the discretized equations on the flow structures, different residual levels are used in simulations, e.g. the residual levels of 1×10^{-3}, 1×10^{-4}, 1×10^{-5} and 1×10^{-5} with 50 inner iterations. The residuals 1×10^{-3} and 1×10^{-4} adopt the default number of inner iterations (20) for the inner loop stopping criteria, and the inner loop at each time step can reach the set residual convergence criteria. However, at the residual level of 1×10^{-5} the solutions cannot reach the set residual convergence requirements within the nominated number of inner iterations, resulting in the residual level 1×10^{-5} acting as 1×10^{-4}. To clarify the effect of further reducing the residual level on the simulation results, the number of the inner iteration was increased to 50 (helps further reduce the residuals), i.e. the residual level of 1×10^{-5} with 50 inner iterations.

Figs. 15(a), (d), (g) and (j) show the contours of mean flow field at residual levels 1×10^{-3}, 1×10^{-4}, 1×10^{-5} and 1×10^{-5} with 50 inner iterations. Similar to the effect of the time step, the mean flow field obtained from different residual levels are almost identical to flow state I, except that the shape and size of the upper elliptical vortex are slightly different. This can also be inferred from the pressure coefficient distribution (see Fig. 16) and the corresponding pressure coefficient torus at different residual levels (see Fig. 17). In addition, with the instantaneous flow fields a series of smaller vortices can be observed, as shown in Figs. 15(b), (e), (h) and (k). However, compared with Figs. 15(c), (f), (i) and (l), the flow field structures observed at the residual level 1×10^{-3} are relatively poorly resolved. This is because a larger residual level is used, meaning a large iteration error is brought in.

Fig. 18 presents the vortex centre at different residual levels. For the saddle point S, the upper elliptical vortex core C and the triangular vortex core B, the differences at different residual levels are large. The locations of the upper elliptical vortex core C at the residual levels 1×10^{-5} and 1×10^{-5} with 50 inner iterations are closer to the experimental results compared to the others; while for the bottom triangular vortex core B, the residual levels 1×10^{-3} and 1×10^{-4} show better agreement with the experiment. Overall, the vortices and saddle point match well with the experiments.

Fig. 19 compares the streamwise and vertical velocity distributions in the near wake at different residual levels. Small differences are observed in the velocity profiles at different residual levels but with the identical trends. Compared to the effect of the time steps, the effect of the residual levels contributes to a smaller discrepancy.

Table 4 shows the mean drag and lift coefficients at different residual levels. For the $\langle C_x \rangle$ and $\langle C_z \rangle$, no significant variation can be observed at different residuals. For example, both of the maximum $\langle C_x \rangle$ and $\langle C_z \rangle$ appear at residual level 1×10^{-5} with 50 inner iterations, while both of the minimum occur at the residual level 1×10^{-4}. The difference of $\langle C_x \rangle$ and $\langle C_z \rangle$ at four cases is about 0.4% and 1.3%, respectively. Thus, considering the error caused by residual level 1×10^{-3}, the residual level 1×10^{-4} with default inner iterations was used for the following analysis.

3.4 Influence of momentum discretization schemes

In this section, the impact of the momentum discretization schemes on the flow structures around the GTS is investigated at the residual level of 1×10^{-4} with the default inner iterations. The bounded central differencing discretization scheme is usually recommended for momentum discretization in IDDES [38]. Herein, the main purpose is to study the influence of the second-order upwind scheme in IDDES simulation.

Figs. 20(a) and (d) are the contours of the mean velocity fields using different momentum discretization schemes. The second-order upwind scheme cannot predict the upper elliptical vortex as well, and its triangular vortex at the bottom is smaller, compared with the bounded central differencing scheme. Also, its ground vortex is larger, higher and closer to the base. Examining the instantaneous flow fields in both schemes shows that a series of

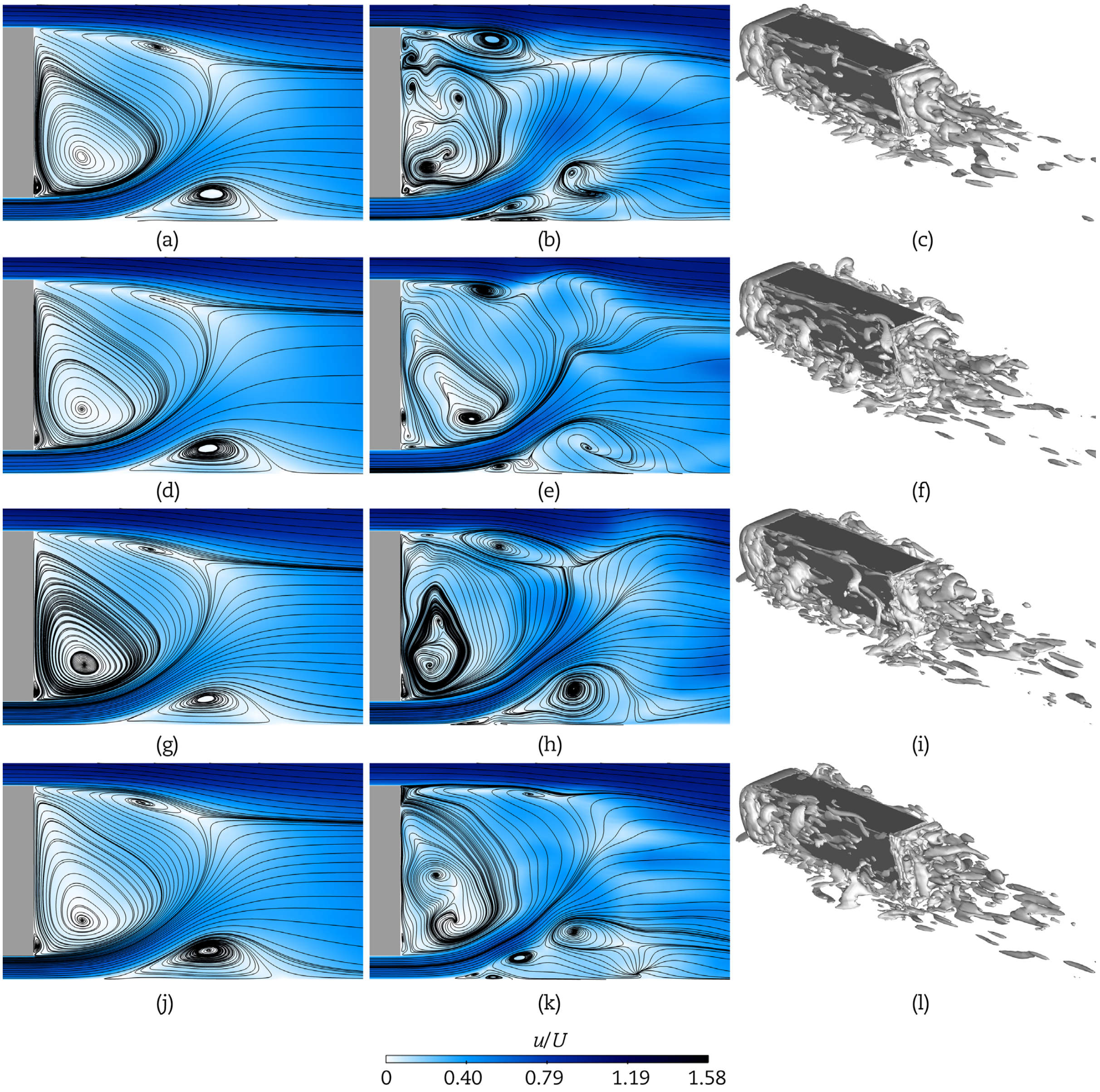

Fig. 15. The normalized time averaged velocity field for residual level of (a) 1×10^{-3}, (d) 1×10^{-4}, (g) 1×10^{-5}, (j) 1×10^{-5} with 50 inner iterations; the normalized instantaneous velocity field for residual level of (b) 1×10^{-3}, (e) 1×10^{-4}, (h) 1×10^{-5}, (k) 1×10^{-5} with 50 inner iterations; the iso-surface of Q-criterion ($Q = 1\times10^{4}$ s^{-2}) for residual level of (c) 1×10^{-3}, (f) 1×10^{-4}, (i) 1×10^{-5}, (l) 1×10^{-5} with 50 inner iterations.

vortices are located around the large dominant vortices shown in the mean flow (see Figs. 20(b) and (e)). However, as shown in Figs. 20(c) and (f), the flow predicted by the second-order upwind scheme only captures these large-scale structures, and more of the small-scale structures are captured in the simulation using the bounded central differencing scheme. Theoretically, the second-order accurate data can be obtained by the second-order upwind scheme. However, from these results, the second-order upwind scheme generates a false diffusion in IDDES, which influences the fidelity of the computational flow field.

Fig. 21 shows the contour of the pressure coefficient in different momentum discretization schemes. The base pressure under the second order upwind scheme is lower compared to the bounded central differencing scheme. Fig. 22 shows the pressure coefficient torus behind the GTS closer to the base with the second-order upwind scheme. Also shown in that, there is a smaller torus with a larger inclination angle when using the bounded central differencing scheme, which can explain the reason of the base pressure distribution. The large differences in the force coefficients when using the two different schemes are shown in Table 5. The second-order upwind scheme can lead to larger forces. For the lift force, the second-order upwind scheme predicts a 3.0% increase, while for the drag force, the difference of them increases to 6.5%.

Fig. 23 shows the streamwise and vertical velocity distributions in the near wake under different momentum discretization schemes. At $X/H \leq 0.75$ the discrepancy of velocity distributions between the two discretization schemes is evident, especially those near the ground. However, at $X/H > 0.75$, there is not much difference between them, with only some small fluctuations.

Taking all these factors into account, the discretization schemes clearly have an obvious influence on the wake flow topology, base pressure and aerodynamic forces. The bounded central differencing scheme is recommended for use in the discretization of the momentum equation in IDDES simulation.

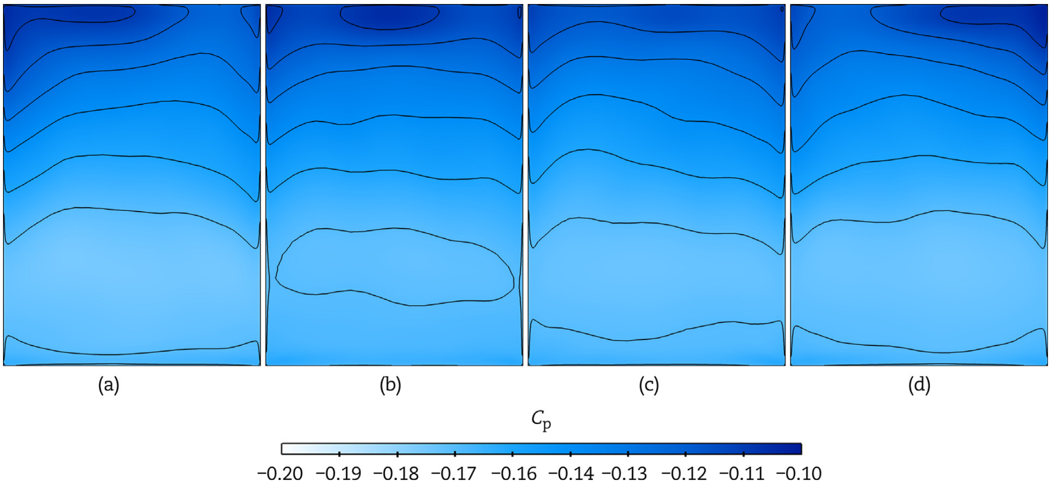

Fig. 16. Mean pressure coefficient C_p distribution on the base for (a) residual level of 1×10^{-3}; (b) residual level of 1×10^{-4}; (c) residual level of 1×10^{-5}; (d) residual level of 1×10^{-5} with 50 inner iterations.

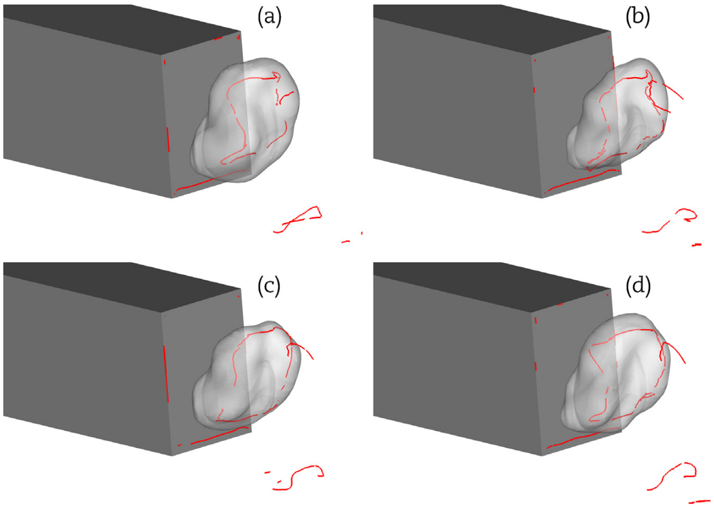

Fig. 17. Visualization of the iso-surfaces of C_p for (a) residual level of 1×10^{-3}; (b) residual level of 1×10^{-4}; (c) residual level of 1×10^{-5}; (d) residual level of 1×10^{-5} with 50 inner iterations, $C_p = -0.18$ in all these cases. (The red lines indicate the time-averaged vortex cores.)

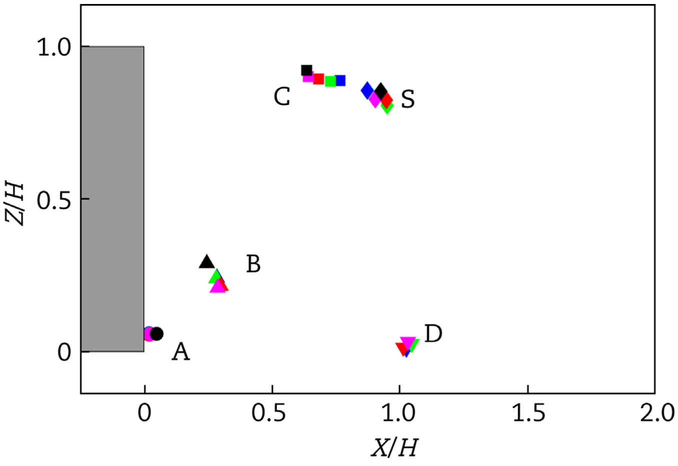

Fig. 18. Centre location of the time-averaged vortices. The residual level 1×10^{-3} (green), the residual level 1×10^{-4} (blue), the residual level 1×10^{-5} (red) and the residual level 1×10^{-5} with 50 inner iterations (pink) are compared with the experiments [3] (black).

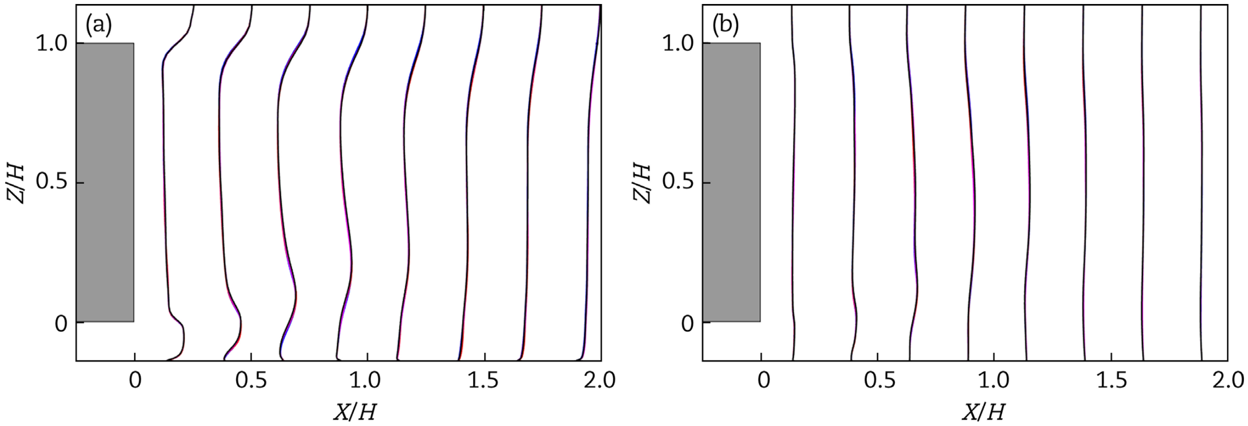

Fig. 19 Comparison of (a) streamwise velocity and (b) vertical velocity profiles. (The red, blue, pink and black lines correspond to the residuals of $1{\times}10^{-3}$, $1{\times}10^{-4}$, $1{\times}10^{-5}$ and $1{\times}10^{-5}$ with 50 inner iterations, respectively.)

Table 4. Time-averaged force coefficients on the GTS model at different residual levels.

Residual level	$\langle C_x \rangle$	$\langle C_z \rangle$
$1{\times}10^{-3}$	0.5637	−0.2239
$1{\times}10^{-4}$	0.5629	−0.2212
$1{\times}10^{-5}$	0.5638	−0.2223
$1{\times}10^{-5}$ (50 inner iterations)	0.5653	−0.2242

3.5 Influence of turbulence models

The simulation results of using different turbulence models, e.g. IDDES and URANS, are compared in this section. Considering the flexibility of turbulence models, some numerical set-ups are not identical. For example, in URANS simulations, the bounded central differencing scheme cannot be used, so the second-order upwind scheme (recommended by solver) is applied in the momentum discretization. To minimize the influence of the grid resolution on the numerical results, all simulations in this section were performed on the fine grid.

Fig. 24 shows the mean flow field using different turbulence models. Compared with figure 5 of Ref. [3], the URANS simulations do not accurately capture the shape and the size of the dominant vortices, although the similar asymmetric flow topology can be observed. For example, the upper elliptical vortex and the ground vortex are larger, while the bottom triangular vortex is smaller. This is because in IDDES the LES treatment is employed for the core turbulent region, while the unsteady RANS models are applied to the near-wall region. The large turbulence in the separated region will be resolved explicitly in IDDES, whereas in URANS all turbulence is modelled. Therefore, the IDDES has a better capacity to predict the flow topology than URANS.

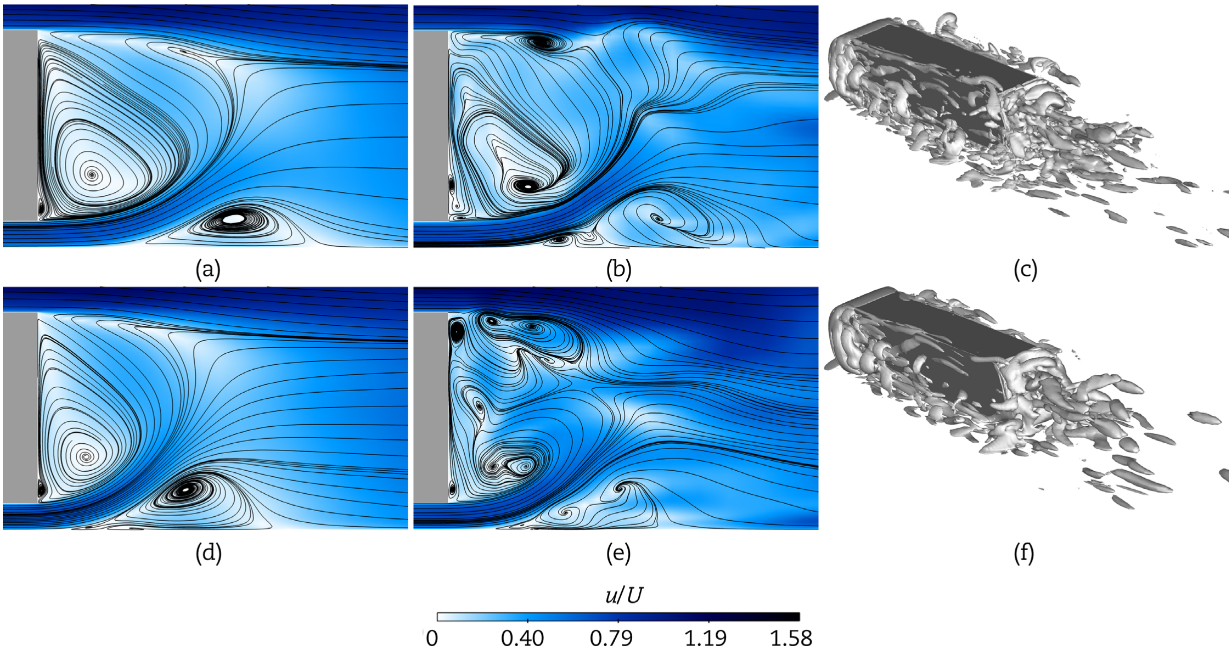

Fig. 20. The normalized time averaged velocity field for (a) the bounded central differencing scheme, (d) the second-order upwind scheme; the normalized instantaneous velocity field for (b) the bounded central differencing scheme, (e) the second-order upwind scheme; the iso-surface of Q-criterion ($Q = 1{\times}10^4$ s^{-2}) for (c) the bounded central differencing scheme, (f) the second-order upwind scheme.

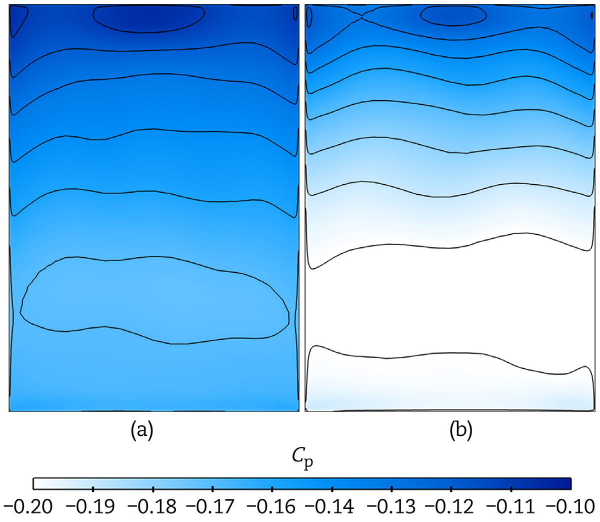

Fig. 21. Mean pressure coefficient C_p distribution on the base for (a) the bounded central differencing scheme; (b) the second-order upwind scheme.

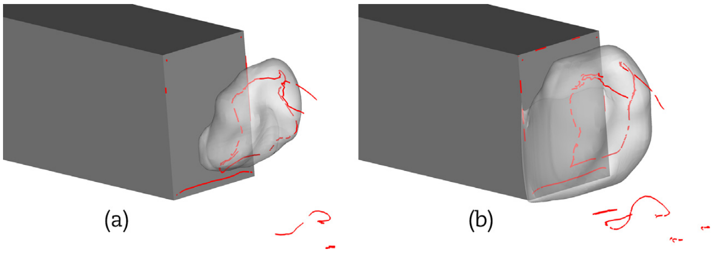

Fig. 22. Visualization of the iso-surfaces of the C_p for (a) the bounded central differencing scheme; (b) the second order upwind scheme, $C_p = -0.18$ in all these cases. (The red lines indicate the time-averaged vortex cores.)

Table 5. Time-averaged force coefficients on the GTS model in different momentum discretization schemes.

Momentum discretization schemes	$\langle C_x \rangle$	$\langle C_z \rangle$
Bounded central differencing	0.5629	−0.2212
Second-order upwind	0.5995	−0.2278

Fig. 25 shows the C_p distribution in different turbulence models. Due to the differently resolved levels in different turbulence models, the corresponding wake flows are not the same. Using the same pressure coefficient cannot show the torus clearly. Therefore, different pressure coefficients are selected for the comparison between two turbulence models. The base pressure distribution in the URANS simulation shows a higher-pressure region in the middle of the base, with the surroundings showing lower

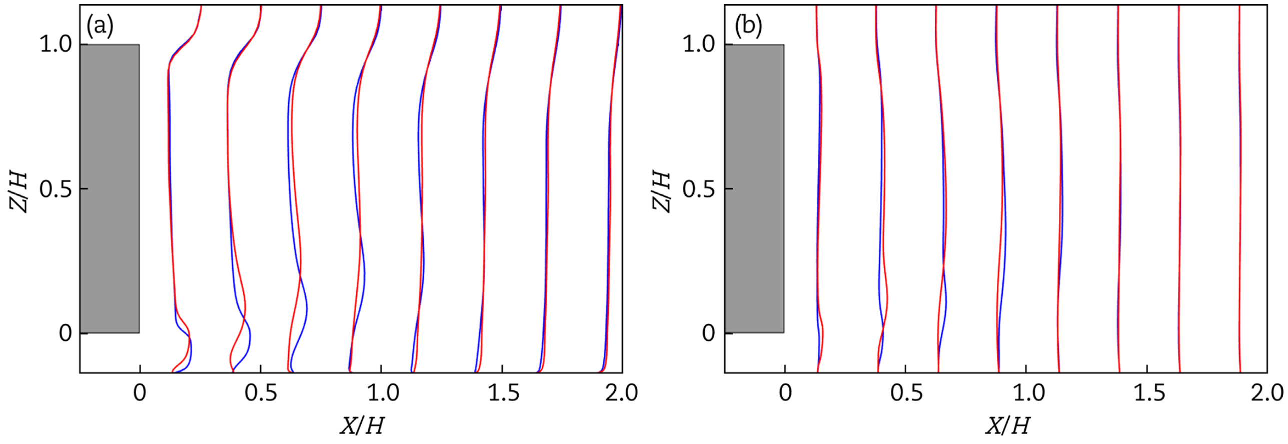

Fig. 23. Comparison of (a) streamwise velocity and (b) vertical velocity profiles. (The blue and red lines correspond to bounded central differencing scheme and second order upwind scheme, respectively.)

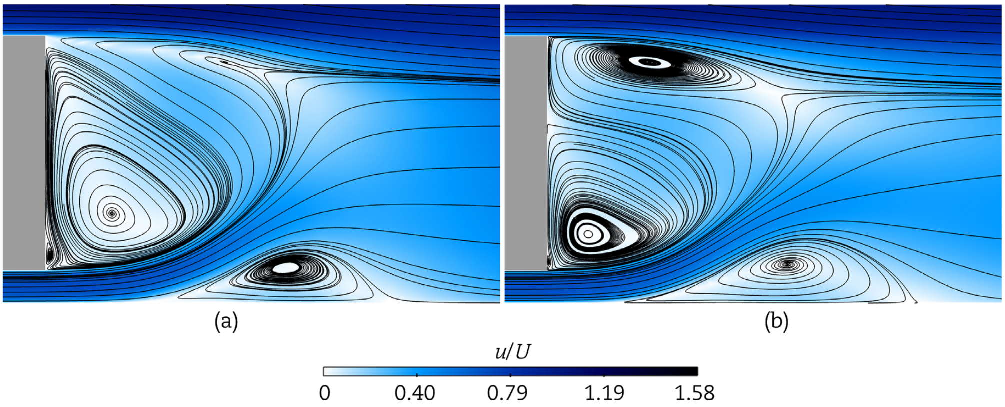

Fig. 24. Visualization of the time-averaged velocity field using different turbulence models: (a) IDDES; (b) URANS.

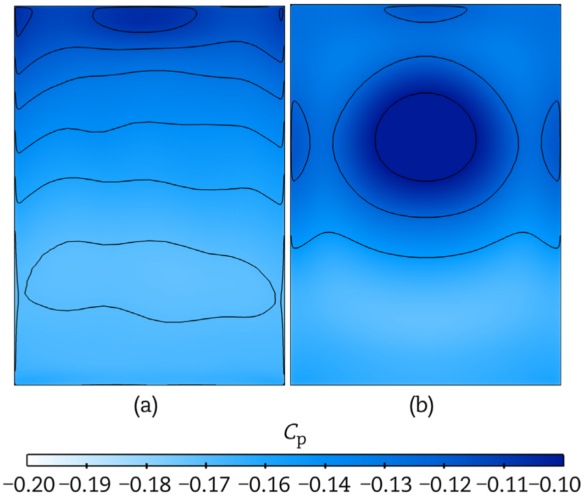

Fig. 25. Mean pressure coefficient C_p distribution on the base in (a) IDDES; (b) URANS.

pressure. This indicates that the vortices are closer to the base with URANS. The results in Fig. 26 show that with URANS there is a hole in the centre of the pressure coefficient torus, and the torus is much closer to the base, especially the bottom part. In addition, the torus and vortex cores in URANS are smoother than those for IDDES. This can be ascribed to the Reynolds averaging, which masks the small turbulence fluctuations.

The centre locations of the time-averaged vortices are shown in Fig. 27. The vortex cores and saddle points in URANS show a large difference with IDDES and experiments. The positions in IDDES agree well with the experimental data given by McArthur et al. [3]. Comparison of the lift and drag force coefficients is listed in Table 6. These show that compared to the IDDES the URANS predicts a 3.0% lower drag coefficient, while the difference approaches 13.0% for the lift force. Fig. 28 shows the streamwise and vertical velocity distributions in the near wake with the different turbulence models. From the above analysis, it can be deduced that the velocity distributions in URANS (red line) have differences with the IDDES, especially for streamwise velocity located between $X/H < 0.5$ and $X/H > 1.5$.

Therefore, the URANS can predict the asymmetry but far from the flow state I observed in the experiment of Ref. [3]. The time-averaged force coefficients and the locations of the vortices further confirmed that large differences are observed between the predictions. To resolve this bimodal flow topology a time-dependent approach such as IDDES is a better alternative choice.

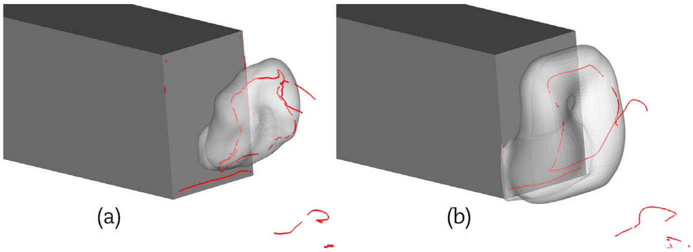

Fig. 26. Visualization of the iso-surfaces of C_p (a) IDDES, $C_p = -0.18$; (b) URANS, $C_p = -0.15$. (The red lines indicate the time-averaged vortex cores.)

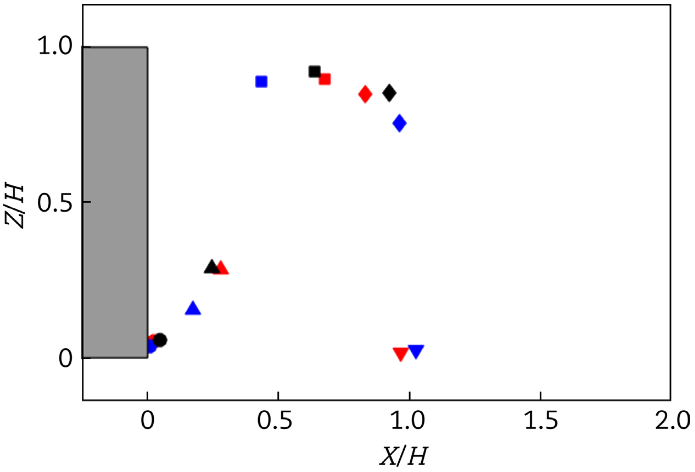

Fig. 27. Centre location of the time-averaged vortices. (URANS (blue), IDDES (red) are compared with the experiments of Ref. [3] (black).)

Table 6. Time-averaged force coefficients on the GTS model at different turbulence models.

Turbulence models	$\langle C_x \rangle$	$\langle C_z \rangle$
IDDES	0.5629	−0.2212
URANS	0.5462	−0.2500

4. Conclusions

For these simulations, the choice of computational parameters, e.g. the grid resolution, time step, residual level and momentum discretization schemes, has a verifiable effect on the wake flow topology of the GTS at $Re = 2.7\times10^4$ using IDDES. Verification was provided by direct comparison with experiments [3], LES [4], PANS [5] and URANS. This provides a clear guidance on how to make choices on the simulation parameters and also on how to assess the ability of IDDES to predict such flow topologies. The findings are summarized as follows.

On the medium and fine meshes, the flow topologies observed are consistent with those shown in previous experiments (denoted as flow state I). The flow topology on the coarse mesh retains the asymmetry but shows a large difference from the results found with LES and PANS (denoted as flow state II) according to the quantitative analysis. This can be ascribed to the insufficient spatial resolution for capturing the flow structures. This phenomenon agrees with the properties of IDDES, where there can be a switch between URANS and LES by comparing the length scale of turbulence and mesh spacing. On the coarse mesh, the IDDES plays the role of URANS, resulting in a large discrepancy. Therefore, a finer mesh is required when the IDDES is used to predict this asymmetric flow topology.

Considering the effects of time steps, the flow structures, except for the location of the upper vortex core and the saddle point at the time step of 1×10^{-3} s, remain identical. With decreased time steps the drag and lift coefficients finally tend to be stable. For different residuals the whole flow structures are slightly different. The differences in drag coefficient and lift coefficient between different residuals are within 2%. Considering the trade-off between computing resources and accuracy, the time step of 1×10^{-4} s and residual level of 1×10^{-4} are recommended. For momentum discretization schemes, the second-order upwind scheme in IDDES fails to accurately predict some of the primary flow structures, while the bounded central discretization scheme shows good agreement with the experiments of Ref. [3]. For the differences arising from different turbulence models, it is found that although the flow structures predicted by URANS can be asymmetrical, the shape, size and locations of the vortex cores can be quite different from those seen in experiments;

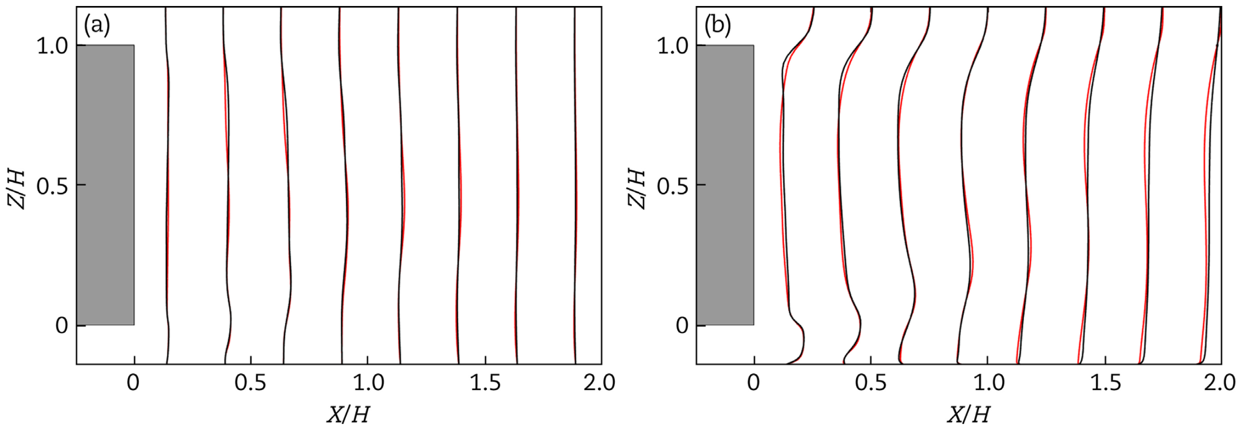

Fig. 28. Comparison of (a) streamwise velocity and (b) vertical velocity profiles. (The red and black lines correspond to URANS and IDDES, respectively.)

the IDDES gives a more accurate prediction compared with the experiments.

This study provides a detailed assessment about the impacts of computational parameters on the flow topology around the GTS and proves that the IDDES method is highly applicable for this flow field. This knowledge is expected to help others perform more accurate simulations for the GTS flows.

Fundings

This work was supported by the Initial Funding of Specially appointed Professorship of Central South University, China (Grant No. 202045014) and Natural Science Foundation of Hunan Province, China (Grant No. 2020JJ4737).

Acknowledgements

The authors acknowledge the computing resources provided by the High-Speed Train Research Center and the High Performance Computing Center of Central South University, China. The authors also acknowledge the LES results provided by Dr Anirudh N. Rao.

Disclosure statement

No potential conflict of interest was reported by the authors.

References

1. Croll R H, Gutierrez W T, Hassan B et al. Experimental Investigation of the Ground Transportation Systems (GTS) Project for Heavy Vehicle Drag Reduction. *International Congress & Exposition of the Society of Automotive Engineers* 1996;237–259.
2. Hassan B, Gutierrez W, Wolfe W et al. Numerical prediction of aerodynamic drag for heavy ground transportation vehicles. *13th Applied Aerodynamics Conference* 1995;1238–1248.
3. McArthur D, Burton D, Thompson M C et al. On the near wake of a simplified heavy vehicle. *J Fluids Struct* 2016;**66**:293–314.
4. Rao A N, Zhang J, Minelli G et al. An LES investigation of the near-wake flow topology of a simplified heavy vehicle. *Flow Turbul Combust* 2018;**102**:389–415.
5. Rao A N, Minelli G, Zhang J et al. Investigation of the near-wake flow topology of a simplified heavy vehicle using PANS simulations. *J Wind Eng Ind Aerodyn* 2018;**183**:243–272.
6. Salari K, McWherter-Payne M. *Computational Flow Modeling of a Simplified Integrated Tractor-Trailer Geometry*.United States: Department of Energy,2003;1–49.
7. Salari K, Ortega J, Castellucci P. Computational prediction of aerodynamic forces for a simplified integrated tractor-trailer geometry. *34th AIAA Fluid Dynamics Conference and Exhibit, Fluid Dynamics and Co-located Conferences* 2004;1–45.
8. Storms B, Ross J, Heineck J et al. An experimental study of the ground transportation system (GTS) model in the NASA Ames 7-by 10-ft wind tunnel. National Aeronautics and Space Administration Ames Research Center,2001:1–21.
9. Maddox S, Squires K D, Wurtzler K E et al. Detached-Eddy Simulation of the Ground Transportation System. In: McCallen R Browand F (eds).*The Aerodynamics of Heavy Vehicles II: Trucks, Buses, and Trains*. Berlin:Springer,2004;89–104.
10. Ortega J M, Dunn T, Mccallen R et al. Computational Simulation of a Heavy Vehicle Trailer Wake. In: McCallen R Browand F (eds).*The Aerodynamics of Heavy Vehicles II: Trucks, Buses, and Trains* Berlin:Springer,2004;219–233.
11. Unaune S V, Sovani S, Kim S-E. Aerodynamics of a generic ground transportation system: detached eddy simulation. *SAE Trans* 2005;**114**:596–611.
12. Roy C J, Payne J, McWherter-Payne M. RANS simulations of a simplified tractor/trailer geometry. *J Fluids Eng* 2006;**128**:1083–1089.
13. Ghias R, Khondge A, Sovani S D. Flow simulations around a generic ground transportation system: using immersed boundary method. *SAE Technical Paper* 2008.
14. Roy C J, Ghuge H A. Detached Eddy Simulations of a Simplified Tractor/Trailer Geometry. In: McCallen R Browand F (eds).*The Aerodynamics of Heavy Vehicles II: Trucks, Buses, and Trains*. Berlin:Springer,2009;363–381.
15. Gunes D. On the similarity of wind tunnel experiments and numerical simulation of heavy-duty trailer flow. *Progr Comput Fluid Dyn* 2010;**10**:168–176.
16. Grandemange M, Gohlke M, Cadot O. Bi-stability in the turbulent wake past parallelepiped bodies with various aspect ratios and wall effects. *Phys Fluids* 2013;**25**:095103.
17. Grandemange M, Gohlke M, Cadot O. Turbulent wake past a three-dimensional blunt body. Part 1. Global modes and bi-stability. *J Fluid Mech* 2013;**722**:51–84.
18. Grandemange M, Gohlke M, Cadot O. Turbulent wake past a three-dimensional blunt body. Part 2. Experimental sensitivity analysis. *J Fluid Mech* 2014;**752**:439–461.
19. Grandemange M, Gohlke M, Parezanović V et al. On experimental sensitivity analysis of the turbulent wake from an axisymmetric blunt trailing edge. *Phys Fluids* 2012;**24**:035106.
20. Herry B B, Keirsbulck L, Labraga L et al. Flow bistability downstream of three-dimensional double backward facing steps at zero-degree sideslip. *J Fluids Eng* 2011;**133**:054501.
21. Lawson N J, Garry K P, Faucompret N. An investigation of the flow characteristics in the bootdeck region of a scale model notchback saloon vehicle. *Proceedings of the Institution of Mechanical Engineers Part D Journal of Automobile Engineering* 2007;739–754.
22. Volpe R, Devinant P, Kourta A. Unsteady experimental characterization of the natural wake of a squareback Ahmed model. *ASME 2014 4th Joint US-European Fluids Engineering Division Summer Meeting collocated with the ASME 2014 12th International Conference on Nanochannels, Microchannels, and Minichannels* 2014; 1–9.
23. Volpe R, Devinant P, Kourta A. Experimental characterization of the unsteady natural wake of the full-scale square back Ahmed body: flow bi-stability and spectral analysis. *Exp Fluids* 2015;**56**:99.
24. Cadot O, Evrard A, Pastur L. Imperfect supercritical bifurcation in a three-dimensional turbulent wake. *Phys Rev E* 2015;**91**:063005.
25. Schmidt H J, Woszidlo R, Nayeri C N et al. The effect of flow control on the wake dynamics of a rectangular bluff body in ground proximity. *Exp Fluids* 2018;**59**:107.
26. Hassan M, Badlani D, Nazarinia M. Numerical study of the effect of aspect ratio on the flow characteristics of the Ground Transportation System. *J Wind Eng Ind Aerodyn* 2020;**206**: 104314.
27. Shur M L, Spalart P R, Strelets M K et al. A hybrid RANS-LES approach with delayed-DES and wall-modelled LES capabilities. *Int J Heat Fluid Flow* 2008;**29**:1638–1649.
28. Spalart P R. Detached-eddy simulation. *Annu Rev Fluid Mech* 2009;**41**:181–202.
29. Sun Z K, Wang T T, Wu F. Numerical investigation of influence of pantograph parameters and train length on aerodynamic drag of high-speed train. *J Central South Univ* 2020;**27**: 1334–50.

30. Wang J, Minelli G, Miao X et al. The Effect of Bogie Positions on the Aerodynamic Behavior of a High-Speed Train: An IDDES Study. *Flow Turbul Combust* 2021;**107**:257–282.
31. Minelli G, Yao H D, Andersson N et al. An aeroacoustic study of the flow surrounding the front of a simplified ICE3 high-speed train model. *Appl Acoust* 2020;**160**:107125.
32. Munoz-Paniagua J, García J, Lehugeur B. Evaluation of RANS, SAS and IDDES models for the simulation of the flow around a high-speed train subjected to crosswind. *J Wind Eng Ind Aerodyn* 2017;**171**:50–66.
33. Niu J, Wang Y, Chen Z et al. Numerical study on the effect of braking plates on flow structure and vehicle and enhanced braking of vehicles inside and outside tunnels. *J Wind Eng Ind Aerodyn* 2021;**214**:104670.
34. Wang S, Avadiar T, Thompson M C et al. Effect of moving ground on the aerodynamics of a generic automotive model: the DrivAer-Estate. *J Wind Eng Ind Aerodyn* 2019;**195**: 104000.
35. Fan Y, Xia C, Chu S et al. Experimental and numerical analysis of the bi-stable turbulent wake of a rectangular flat-backed bluff body. *Phys Fluids* 2020; **32**:105111.
36. Guilmineau E, Deng G B, Leroyer A et al. Assessment of hybrid RANS-LES formulations for flow simulation around the Ahmed body. *Comput Fluids* 2018;**176**:302–319.
37. Barsotti D L, Divo E A, Boetcher S K S. Optimizing Jets for Active Control of Wake Refinement for Ground Vehicles. *J Fluids Eng Trans ASME* 2015;**137**:121108.
38. Ansys_Inc. ANSYS FLUENT User's Guide 19.2. 2019.